Characterisation of the ventilation in a Taylor-Couette setup with surface piercing riblets

Adrien Clement, Blandine Barabe, Celine Gabillet

Characterisation of the ventilation in a Taylor-Couette setup with surface piercing riblets

A. CLEMENT[a], B. BARABE[a], C. GABILLET[a]

a. Institut de Recherche de l'Ecole Navale
corresponding author: adrien.clement@ecole-navale.fr

Abstract :

For free surface-Piercing structures (FSPS) submitted to high speed flows, such as propellers, hydrofoils of naval vessels or submarine periscopes, ventilation can occur. Ventilation is characterized by air entrapment in low pressure regions and a modification of the free surface waves. A need for a better understanding of the ventilation phenomenon and it's impact has arisen with the general increase of vessels speeds.

Experiments on ventilation have been conducted in a free surface Taylor Couette device, with obstacles attached at the rotating inner cylinder, built for this purpose. In this closed set-up, a sustainable air cavity develops downstream the obstacles. The overall shape of the cavity (depth, length and area coverage) has been characterized by image processing for different Reynolds number.

The device makes it possible to reproduce same kind of air cavity's shape as expected for ventilation along the suction side of a free surface piercing hydrofoil. When increasing the rotating velocity, fully wetted, partially ventilated and then fully ventilated flows are successively observed. A further study is on the way to test the impact on the dynamics of the ventilation and transitions between flow conditions using a super-hydrophobic coating applied on the inner cylinder and the results will be presented at the conference.

Keywords: Free Surface-Piercing Structures, Taylor-Couette flow, Turbulence, Air cavity, Ventilation

1 Introduction

For free surface-Piercing structures (FSPS) submitted to high speed flows, such as propellers, hydrofoils of naval vessels or submarine periscopes, ventilation can occur. Ventilation is characterized by air entrapment in low pressure regions and a modification of the free surface waves. It can drastically modify the performances and controllability of the vessels by changing the hydrodynamic forces applied on FSPS, as well as their hydro-elastic response under flow excitation [1]. A need for a better understanding of the ventilation phenomenon and its impact has arisen with the general increase of vessels speeds. It also raises the question of the influence of wettability of FSPS on their ability to ventilate. Most of the hydrodynamic studies dedicated to super-hydrophobic surfaces were rather focused on their ability to reduce viscous drag in turbulent flows [2], rather than on their ability to capture and discharge air when

the super-hydrophobic surface ventilates. Rothblum, [3] has analyzed the influence of different roughness and coatings on the ventilation of a surface piercing strut but no clear influence of the wettability has been evidenced. Some few studies have been dedicated to the influence of surface wettability on cavitation inception and vapor cavity size [4, 5] but they show no clear trends. Today, there is obviously a need in conducting experimental investigations of the ventilation process and its dynamics in the closure region for different wetting properties of free surface-Piercing structures in a fully controlled apparatus. In a closed Taylor Couette set-up, which generates a rotating flow in the gap between two coaxial cylinders, it is possible to obtain a sustainable air cavity downstream obstacles attached at the rotating cylinder [6]. The present work aims to describe first measurements of ventilation achieved in a new Taylor Couette device with riblets, built at the French Naval Academy. One specificity of this device is its ease in disassembling the inner cylinder to test cylinders with different wetting properties. For the purpose of ventilation analysis, a home-made image processing method has been developed. First measurements have been performed with a hydrophilic surface made of anodized aluminum. First section presents the experimental set-up: the device and the acquisition and processing methods. The second section presents first results and discussion about the regimes of ventilation and the evolution of the cavity shape and cavity coverage ratio with the Reynolds number.

2 Experimental setup

2.1 Taylor Couette and riblets

The Taylor Couette flow consists of a flow confined between two coaxial cylinders. In our setup, the inner cylinder of radius $R_i = 50$ is rotating at the angular velocity ω, which can be varied. The geometrical characteristics of the apparatus used for this study are summarized in (Table:1). The tested inner cylinder is made of anodized aluminum, while the outer cylinder is made of Plexiglas.

The device (Figure:1a) is characterized by a gap width $d = 20\,\mathrm{mm}$, a radii ratio of $R_i/R_o = 0.71$ and an aspect ratio $L/d = 16$, with L being the height of the inner cylinder. The gap is filled partially with deionized water and the free surface height h, measured from the bottom of the inner cylinder, can be varied. In this study, only one value of h has been investigated ($h = 71\,\mathrm{mm}$). h_i and h_o stand for the heights of the free surface at the contact line with the inner and outer cylinders respectively (Figure:1a). When the inner cylinder rotates, h_i and h_o are different due to the pressure difference induced by the azimuthal flow.

Two free surface piercing obstacles, made of axial square riblets are attached to the inner cylinder at opposing azimuthal positions. The riblet width is $e = 2.5\,\mathrm{mm}$, which corresponds to 12.5% of the gap width. One specificity of the device is its ease in disassembling the inner cylinder to test cylinders with different wetting properties, with or without riblets. A general sketch of the device as well as a sketch of the inner cylinder with riblets is shown in (Figure:1a,1b). The riblets are introduced to generate air entrapment (ventilation) along the inner cylinder, in the pressure defect region, downstream the riblets. In our study, the ratio e/δ_0 of the riblet width to the undisturbed boundary layer thickness is in the range $[6\ ;\ 11]$. δ_0 is the estimated thickness of the boundary layer without riblets. For turbulent boundary layers, Bradshaw & Wong [7] have classified the strength of the perturbation at a wall according to the value of e/δ_0. For $e \gg \delta_0$ the flow can be overwhelmingly considered as a perturbed flow, and the flow downstream the obstacle becomes a wake mixing layer.

The characteristic non-dimensional parameters that control the flow are the Reynolds, Taylor and Froude

numbers. The Reynolds number is defined based on the inner cylinder's azimuthal velocity U_i and the gap width d.

$$U_i = R_i\omega;\ Re_d = \frac{U_i d}{\nu} \tag{1}$$

With ν the kinematic viscosity of the water at the operating temperature ($\nu = 1.06 \times 10^{-6}\,\mathrm{m\,s^{-2}}$ at $17.7\,^{\circ}\mathrm{C}$). The temperature is monitored during the tests and showed no major evolution around $17.7\,^{\circ}\mathrm{C}$. The Taylor number Ta is a correction of the Reynolds number that takes into account curvature effect:

$$Ta = \frac{\omega^2 R_i (R_o - R_i)^3}{\nu^2} \tag{2}$$

The characteristics of a ventilated flow varies with the immersed depth-based Froude number Fn_h [1]. Here g is the gravity acceleration.

$$Fn_h = \frac{U_i}{\sqrt{gh}} \tag{3}$$

The operating range of these different non-dimensional parameters is given in (Table:1).

Characteristic		Values	Steps
Height of free surface at rest	h	$71\,\mathrm{mm}$	
Inner Radius	R_i	$50\,\mathrm{mm}$	
Outer Radius	R_o	$70\,\mathrm{mm}$	
Height of the inner cylinder	L	$320\,\mathrm{mm}$	
Rotation speed (RPM)	N	$[260\ ;\ 500]$	20
Reynolds Number (based on gap)	Re_d	$[2.7 \times 10^4\ ;\ 5.2 \times 10^4]$	2×10^3
Taylor Number	Ta	$[3 \times 10^8\ ;\ 1.1 \times 10^9]$	
Froude Number	Fn_h	$[1.7\ ;\ 3.3]$	0.13

Table 1: Characteristics of the setup and non dimensional parameters range of study

2.2 Acquisition and Processing

The gap of the device is illuminated with a LED array which supplies continuous and uniform lightning, at the bottom of the apparatus (Figure:1a). A high speed CCD camera is used to visualize the air cavities developing downstream of the riblets. The axis of the camera is aligned with the meridian plane of the inner cylinder. The field of view of the camera is $155 \times 19.5\,\mathrm{mm}$ along the vertical z and the horizontal x axes, respectively. The scaling factor is $6.6\,\mathrm{px\,mm^{-1}}$. In the zoomed snapshot (Figure:1c), we can see the riblet crossing the median line of the field of view and the bright air cavities downstream.

For each speed, 28123 frames are recorded at 1500fps and these frames are further processed. Acquisitions were done, with and without riblets in order to reconstruct, both the shape of the free surface and the shapes of the cavities. The processing of the video with riblets is done in the following order:

- A tempogram (Figure:2a) is constructed from the median line of each frame, in order to avoid optical distortion from the outer cylinder.
- Some thresholding and noise reductions are applied to the tempogram.

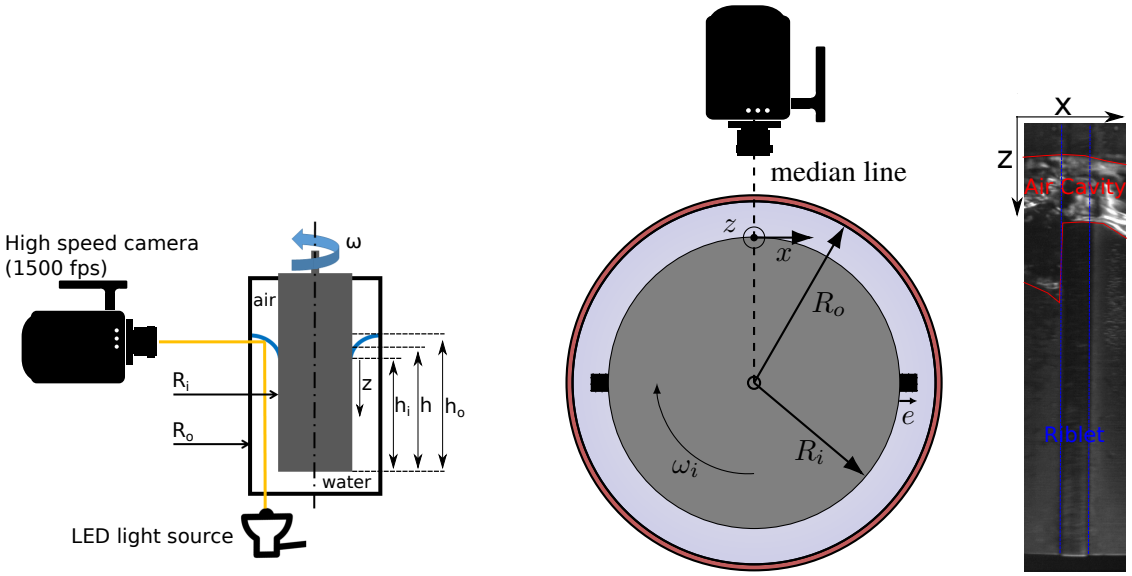

(a) Setup (side view)

(b) Bottom view

(c) Snapshot at N=300rpm

Figure 1: Experimental setup

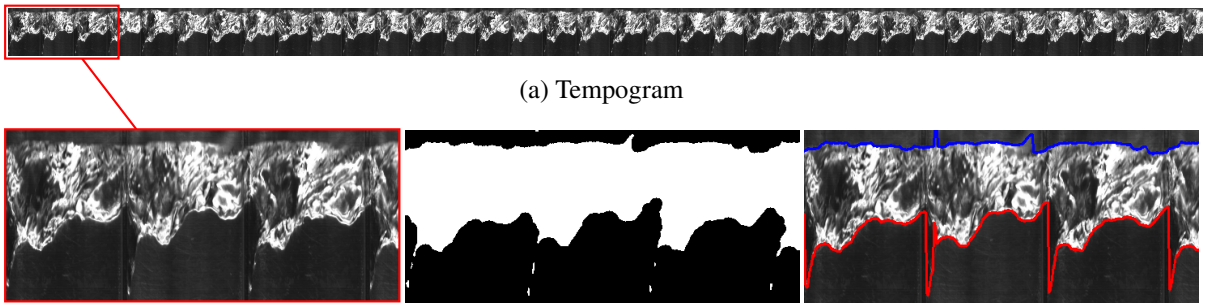

(a) Tempogram

(b) Processing

Figure 2: Image processing applied to the ventilation of the inner cylinder with riblets at 300 rpm

- A pattern matching algorithm (Template Matching Correlation Coefficient) is used to find every occurrence of two cavities, based on the frequency ω of the inner cylinder. The pattern includes both cavity, as it is based on the rotating frequency of the cylinder, this also allows for further discrimination of both riblets.
- The mean pattern of these occurrences is computed and is used to selectively mask the tempogram, to further improve the detection of the cavities (Figure:2b-2).
- Finally, the outline of the cavities are extracted from the binarized tempogram (Figure:2b-3).

3 Analysis

3.1 Free surface and cavity

Visualization of the free surface has been conducted with and without the presence of riblets. A zoom on the tempogram with and without riblets is presented in (Figures:3a and 3b). In order to analyze the

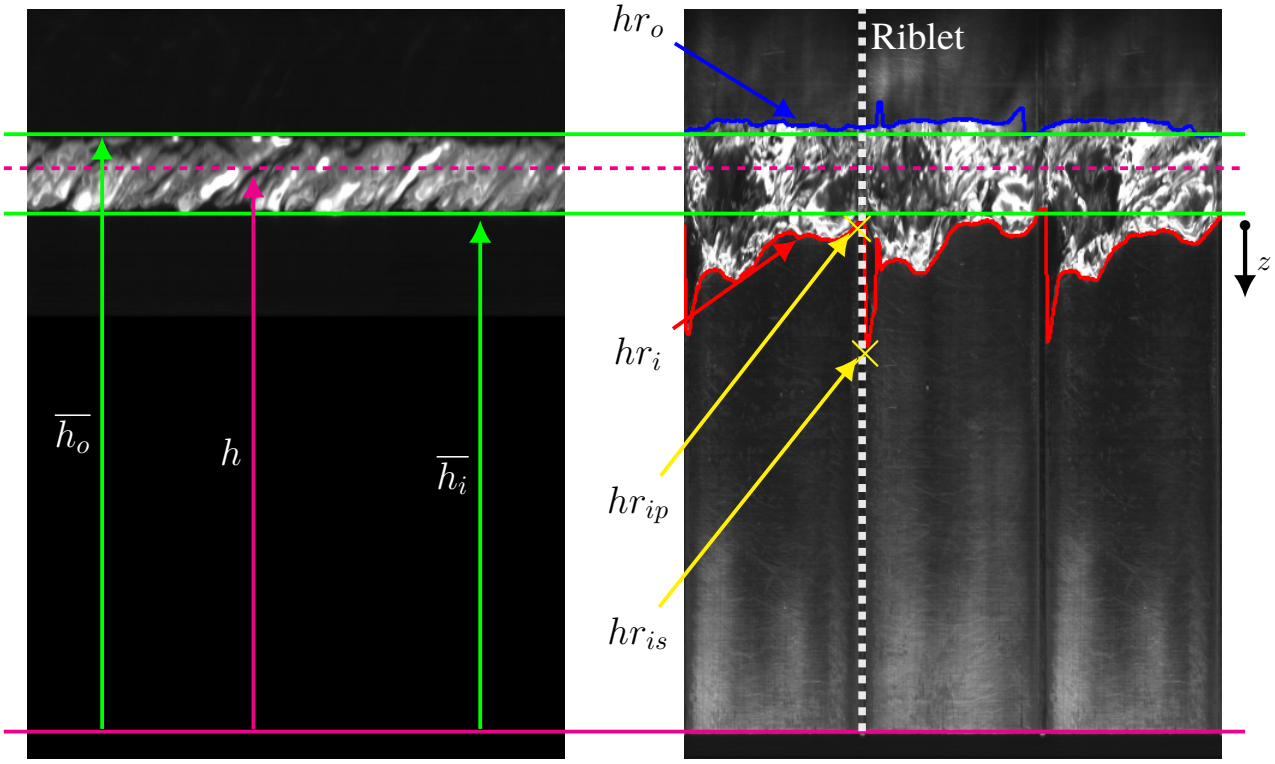

(a) Without riblets

(b) With riblets

Figure 3: Tempogram at 300 rpm. The evolution of the different free surface heights is visible in color (blue and red for inner and outer contact lines of the free surface with the cylinders). One riblet is represented in dashed white. The green lines are the mean heights of the inner and outer free surface without riblets, the original height at rest is plotted in dashed magenta and the bottom of the cylinder is highlighted in magenta

behavior of the air cavities and the free surface, several heights are introduced. All these heights are relative to the position of the bottom of the cylinder.

From the tempogram obtained at the same rotating velocity, without riblets, time averaged heights $\overline{h_i}$ and $\overline{h_o}$ of the free surface in contact with the inner and outer cylinders are measured and plotted in green (Figures:3a). $\overline{h_i}$ is used as a reference for the determination of the depth z of the air cavity, with the riblets. With the riblets, the heights of the free surface in contact with the inner and outer cylinders are denoted as hr_i and hr_o. These heights are plotted in red and blue respectively in (Figures:3b). Their evolution with time $hr_i(t)$ and $hr_o(t)$ has been computed from the tempogram at each operating points.

hr_{ip} and hr_{is} stand for the height of the free surface on the pressure side of the riblet and the height on the suction side of the riblet respectively. They are highlighted by the yellow cross on (Figures:3b). Both hr_{ip} and hr_{is} are determined from the value of $hr_i(t)$, each time a riblet is detected on the tempogram. The maximal depth of the cavity is given by $z_{max} = \overline{h_i} - hr_{is}$.

As can be seen in (Figure:3), ventilation occurs downstream each riblet and has an impact on the overall shape of the free-surface. We can see that the free-surface on the outer cylinder rises to accommodate entrapment of air in the gap $\overline{hr_o} > \overline{h_o}$.

With riblets, at low rotation speeds (Figure:3), the air cavity downstream each riblet doesn't interact with the next riblet and the air cavity doesn't reach the bottom of the cylinder. This regime is referred to as

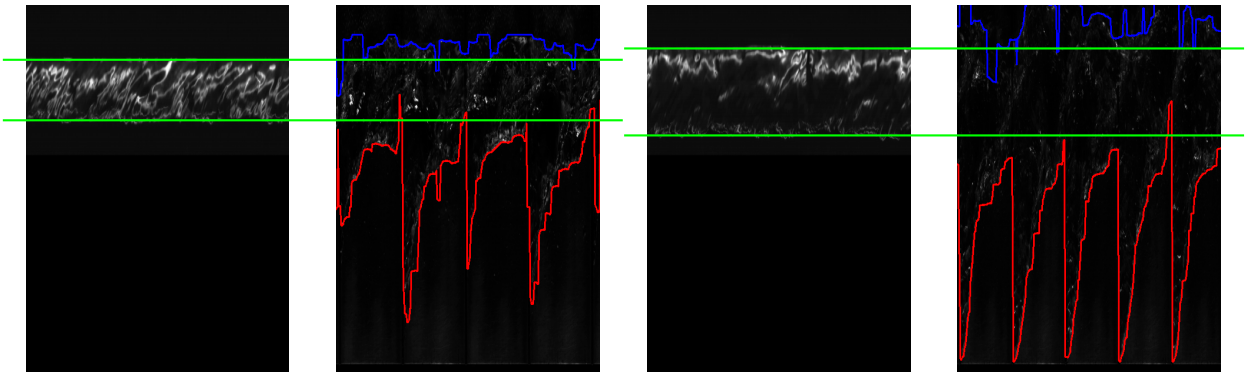

(a) (b) (c) (d)

Figure 4: Tempogram at 420 rpm (a, b) and 500 rpm (c, d), without and with riblets

partially ventilated PV flow. For this regime, the mean height of the free-surface at the inner cylinder in front of the riblet $\overline{hr_{ip}}$ is similar to the height of the free surface without riblets $\overline{h_i}$.

At higher rotation speeds the air cavity interacts with the next riblets and thus the conditions for the initiation of ventilation are modified at the suction side of the next riblet. This phenomenon gives rise to an alternation of the maximal depth of the air cavity hr_{is} for each riblet, as can be seen on the tempogram obtained at a speed of $N = 420\,\mathrm{rpm}$, (Figure:4b). This regime is referred to as the first fully ventilated flow regime ($FV1$).

Finally, at higher speeds, the cavity reaches the bottom of the cylinder on both riblets (Figure:4d) and thus the maximal depth of the cavity stops increasing and saturates. Air entrapment keeps on growing under the inner cylinder, driven by the low pressure. This regime is referred to as the second fully ventilated flow ($FV2$).

For a surface piercing structure, such as for thin lifting surfaces (plates or foils), there exist classically three characteristic flow regimes, referenced as: fully wetted (FW), partially ventilating, and fully ventilating flows. The same terminology can be used for both cavitating and ventilating flows, "ventilating" being replaced with "cavitating" [8].

Flow regime transitions	$FW \rightarrow PV$	$PV \rightarrow FV_1$	$FV_1 \rightarrow FV_2$
N (rpm)	200	420	440
Re_d	2×10^4	4.2×10^4	4.4×10^4
Ta	1.7×10^8	6.9×10^8	7.5×10^8
Fn_h	1.3	2.8	2.9

Table 2: Non-dimensional parameters values at the transition from different ventilated flow regimes in our setup ($h/R_i = 1.42$, $R_i/R_o = 0.71$)

In our setup (Table:2), the fully wetted regime FW is achieved without riblets or with riblets for $N < 200\,\mathrm{rpm}$, which is the rotating velocity for the air cavity inception at the suction side of the riblets. The partially ventilating flow regime PV is obtained when the length of the cavity doesn't reach all the way to the other riblet (for a foil, the cavity doesn't cover all the chord). In our setup, this regime is obtained for rotating speed between 200 and $420\,\mathrm{rpm}$ (Figure:3b). Two different fully ventilated flow regimes states can be considered. FV_1 when the cavity covers the entire chord of a foil (here in the present setup

this is the entire azimuthal span between two riblets) and FV_2 when the cavity reaches the bottom of a foil (here this corresponds to the bottom of the inner cylinder). These two fully ventilated regimes can be seen in (Figure:4b and 4d). FV_1 occurs for rotating speeds between 420 and $440\,\mathrm{rpm}$, while FV_2 is achieved for rotating speeds of $N > 440\,\mathrm{rpm}$. The values of the non-dimensional numbers achieved at these regimes transitions are summarized in (Table:2).

3.2 Ventilation number

The generalized ventilation number can be defined at a depth z beneath the free surface [8]:

$$\sigma_v(z) = \frac{P_\infty(z) - P_{atm}}{\frac{1}{2}\rho U_i^2} = \frac{2gz}{U_i^2} \tag{4}$$

With $P_\infty(z)$ the local pressure under static condition at depth z and P_{atm} the atmospheric pressure.

The pressure defect induced by the riblet can be determined based on the difference between the pressures on the suction side P_s and on the pressure side P_p. When ventilation occurs, this pressure defect can be estimated at the maximal cavity depth $z = z_{max}$ using:.

$$P_p(z_{max}) = P_{atm} + \rho g(\overline{hr_i} - hr_{is}) = P_{atm} + \rho g z_{max} \tag{5}$$

The condition of natural ventilation inception on the suction side, at $z = z_{max}$ yields :
$P_s(z = z_{max}) = P_{atm}$

If the speed of the inner cylinder (U_i) is considered as the reference velocity, the pressure defect coefficient Cp, at z_{max} can be written as:

$$Cp_{min} = \frac{P_s(z_{max}) - P_p(z_{max})}{\frac{1}{2}\rho U_i^2} = \frac{2g(hr_{is} - \overline{hr_i})}{U_i^2} = -\sigma_v(z_{max}) \tag{6}$$

Cp_{min} is considered as the minimum Cp value at ventilation inception point, which is in agreement with the classical law at ventilation or cavitation inception $Cp_{min} = -\sigma$.

The evolution of the ventilation number $\sigma_v(z_{max})$ as a function of the Reynolds number Re_d is plotted in (Figure:5). We have shown the two riblets as there appears to be a difference in the shape of the air cavity between the two riblets. The first riblet is taken as the riblet with the biggest air cavity. Such a difference is due to the mutual influence of the wake of each riblet on the other in the (FV_1) regime. Both riblets show a similar behavior while $Re_d < 4.2 \times 10^4$ and after both cavity have reached the bottom of the cylinder $Re_d > 4.7 \times 10^4$, above $480\,\mathrm{rpm}$.

In (Figure:5), error bars are the amplitude of the root mean square of the ventilation number (standard deviation), computed from all riblets passages detected in the tempogram. These error bars characterize the variability due to reproducibility of the ventilation on each of the riblets. When considering this variability, we can see that the mean value of the ventilation number of both riblets is quite not sensitive to the Reynolds in the PV regime up to $Re_d \sim 4.2 \times 10^4$. Indeed, at the transition from the PV regime to FV_1 regime for riblet number 2, the pressure side of riblet two interferes with the cavity closure region of riblet 1 which increases the variability of the maximal cavity depth of riblet 2 (i.e. the variability of the ventilation number of riblet 2).

In the PV regime, for $Re_d < 4.2 \times 10^4$, the ventilation number is in coincidence with $-Cp_{min}$ of the riblets and, as previously mentioned, it is thus representative of the pressure defect induced by the riblet.

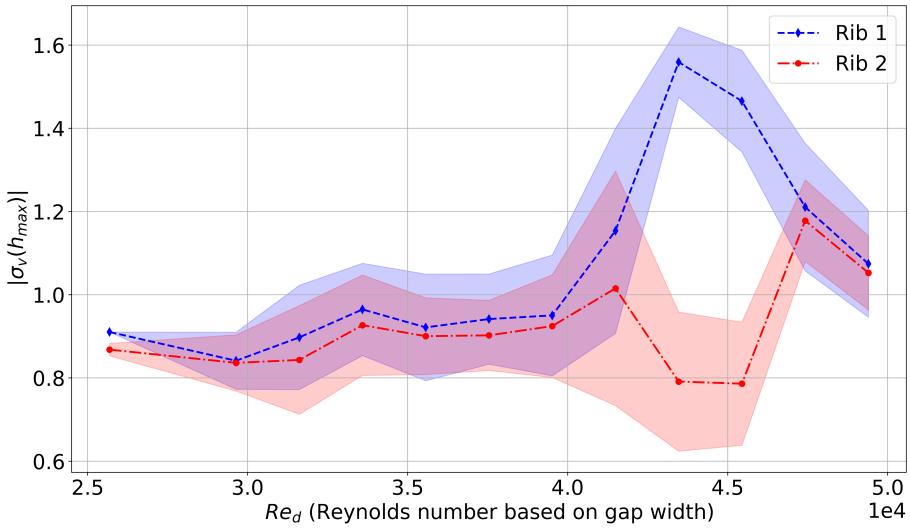

Figure 5: Evolution of the ventilation number

The fact that the Cp_{min} does not scale with the Reynolds number is in agreement with the literature survey. Indeed, for a single-phase Taylor Couette flow, with roughness at the wall, at high Reynolds numbers, the Nusselt number Nu scales with $Ta^{1/2}$ [9]. Nu is the torque ratio between fully turbulent and laminar flows under same condition of temperature and viscosity.

$$Nu = \frac{T_{turbulent}}{T_{laminar}} \propto Re_d \tag{7}$$

Here T is the global torque applied on the inner cylinder. This scaling condition is found in the ultimate turbulent flow regime, where the pressure induced torque is much larger than the viscous induced torque. In Zhu et al. [10], this condition was fulfilled, in a single phase Taylor Couette flow, for a similar geometry as in our experiments (i.e. of same radii ratio and same e/d), in the Re_d range $[8 \times 10^3$; $8 \times 10^4]$.

In the laminar flow range, the torque evolves linearly with ω, thus leading to ($T_{laminar} \propto Re_d$). The global torque is linked to the pressure defect ΔP, and yields according to [9]:

$$T_{turbulent} = N_r \Delta P e h R_i \propto Re_d^2 \tag{8}$$

with N_r the number of riblets Therefore, the exponent of the power scaling law of the non-dimensional pressure defect induced by the riblet in the ultimate turbulent regime is null, which is in agreement with our observations in the PV flow regime for our Reynolds range values:

$$Cp_{min} = \frac{\Delta P}{\frac{1}{2}\rho U_i^2} \propto Re_d^0 \tag{9}$$

3.3 Air cavity

The overall mean shape of the cavity, nondimensionalized by the height of the free surface $\overline{h_i}$ and half the azimuthal perimeter c, is plotted in (Figure:6). We can see that for a rotation speed of $300\,\mathrm{rpm}$, in

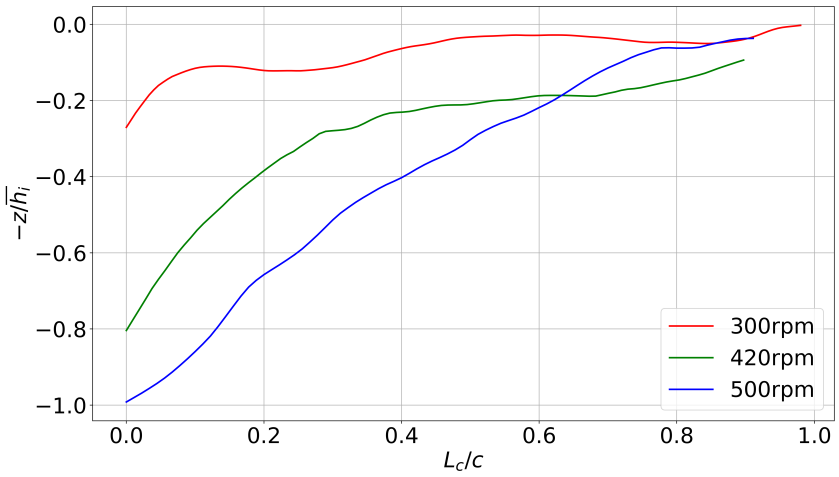

Figure 6: Non-dimensional shape of the air cavity downstream the first riblet (L_c is the length of the cavity in the azimuthal direction, measured at depth z).

the PV flow regime, the cavity doesn't reach the half azimuthal perimeter. For a speed of $420\,\mathrm{rpm}$, the free surface without riblets is higher than the free surface on the pressure side of the second riblet hr_{ip}, the air cavity fully fills the gap between two riblets, we are in the FV_1 flow regime. For a speed of $500\,\mathrm{rpm}$, we are in the FV_2 flow regime, and the cavity reaches both the bottom of the cylinder and the full half perimeter. We can see that the shape of the air cavity is characterized by a relatively linear behavior with z, near the inception point at $z = z_{max}$.

For each rotational speed the angle θ can be introduced, between the horizontal axis and the linear part of the cavity shape, starting at its maximum depth (Figure:7). While $Re_d < 4.2 \times 10^4$, in the PV flow regime, this angle is relatively constant and has a mean value of $32.3°$. The transition from the PV

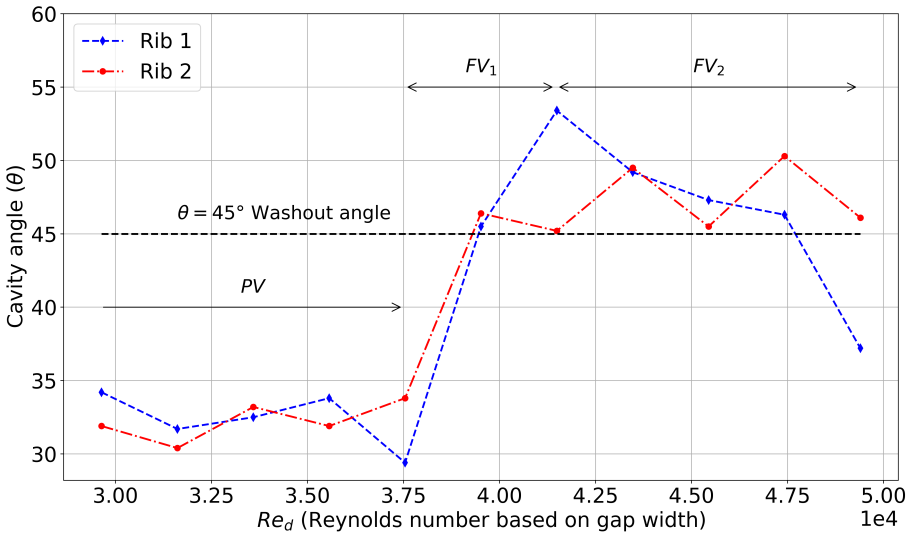

Figure 7: Evolution of the cavity angle (Low Reynolds number are not shown as the angle could not be well calculated)

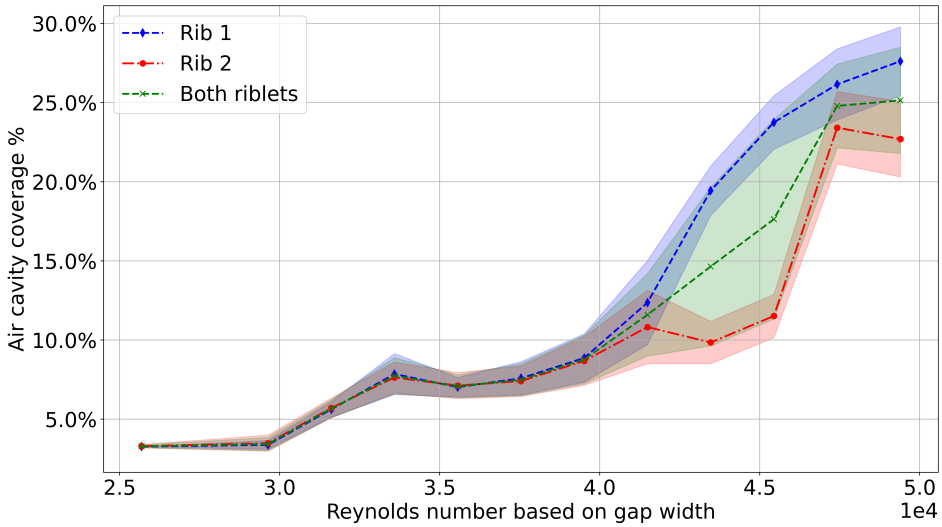

Figure 8: Cover ration of the air cavity

regime to the FV_1 regime is characterized by a sharp increase in this angle, to a mean value of $48.3°$ and $47.4°$ for both riblets respectively, in the FV_1 region. When the FV_2 region is reached $Re_d > 4.4 \times 10^4$, θ becomes dependent on the geometry of the apparatus, as can be seen in (Figure:6). Indeed, the length is limited by half the azimuthal perimeter and the height is limited by the cylinder immersed depth. Thus, in the FV_2 regime, θ starts to decrease, as the height of the free surface h_i decreases with increasing rotation speeds. The influence of the wake of the first riblet delays the transition from FV_1 to FV_2 for the second riblet.

The sharp increase of θ, from $\sim 32°$ to $\sim 48°$ is coherent with what can be found in the literature. According to [8], the washout (the transition between FV flow and PV flow) initiates on a vertical hydrofoil when the angle θ reaches $45°$, defined as the washout angle.

3.4 Coverage ratio

The coverage ratio of the air cavity for one riblet is defined as the ratio between the area of the air cavity $\int_0^{T/2} (\overline{h_i} - hr_i(t))dt$ and the area of the fluid at rest ($\frac{T}{2}\overline{h_i}$). With T the time period for one rotation of the cylinder.

$$\text{Coverage Ratio} = \frac{\int_0^{T/2} (\overline{h_i} - hr_i(t))dt}{\frac{T}{2}\overline{h_i}} \tag{10}$$

The mean value of this coverage ratio is plotted in (Figure:8). It is averaged over every occurrence of the air cavity on each riblet, on the tempogram, over the measurement time. Here, the error bars represent the standard deviation of this value. The coverage ratio shows a sharp increase, starting at $Re_d \sim 4.2 \times 10^4$, which accounts for the transition between the PV and FV_1 flow regimes. At higher speed, when both riblets reach the FV_2 flow regime, the coverage ratio seem to plateau to a value of approximately 25%.

4 Conclusions

In this study, a new experimental apparatus was assessed for the characterization of ventilation induced by a surface piercing structure. The studied apparatus is a Taylor Couette device with a free surface and riblets piercing this free surface in order to initiate ventilation. Special attention has been paid to image processing development to characterize ventilation. Measurements of the maximal cavity depth, cavity shape and cover ratio, for different rotation speeds have shown that the flow regimes scale well with data on foil ventilation from the literature. It is possible to identify the different flow regimes already shown in previous works on surface piercing foils [8], such as the partially ventilated flow regime PV and the fully ventilated flow regimes FV . Non-dimensional flow parameters allow for easy discrimination of these flow regimes.

This work will allow for further analysis of the ventilation of surface piercing structure in a controlled environment. Further work is going to be conducted, regarding the torque of the apparatus and varying the immersed depth of the inner cylinder. Ultimately the apparatus will allow for the study of the influence on ventilated cavities, of both surface roughness and super-hydrophobic coatings applied on the inner cylinder.

Some results on the influence of super-hydrophobic coatings will be shown at the oral presentation.

Acknowledgement

This work has been funded by the French *Agence Nationale de la Recherche (ANR)* under the project *"Du Carbone à l'Or Olympique"*. This work was made possible thank to the facilities of the *Institut de Recherche de L'Ecole Navale (IRENav)* and the support of its staff.

References

[1] Casey M. Harwood et al. "The hydroelastic response of a surface-piercing hydrofoil in multiphase flows. Part 1. Passive hydroelasticity". In: *Journal of Fluid Mechanics* (2019).

[2] Kevin B. Golovin et al. "Bioinspired surfaces for turbulent drag reduction". In: *Philosophical Transactions of the Royal Society A: Mathematical, Physical and Engineering Sciences* 374.2073 (Aug. 2016). Publisher: Royal Society, p. 20160189.

[3] Richard Stone Rothblum. "Investigation of methods of delaying or controlling ventilation on surface piercing struts". Jan. 1977.

[4] Kaoruko Onishi, Kunimasa Matsuda, and Kazuyoshi Miyagawa. "Influence of Hydrophilic and Hydrophobic Coating on Hydrofoil Performance". In: *International Symposium on Transport Phenomena and Dynamics of Rotating Machinery (ISROMAC 2017)*. Maui, United States, Dec. 2017.

[5] Jiafeng Hao, Mindi Zhang, and Xu Huang. "Experimental Study on Influences of Surface Materials on Cavitation Flow Around Hydrofoils". In: *Chinese Journal of Mechanical Engineering* 32.1 (May 2019), p. 45.

[6] Ruben A. Verschoof et al. "Air cavities at the inner cylinder of turbulent Taylor-Couette flow". In: *International Journal of Multiphase Flow* (2018).

[7] P Bradshaw and FYF Wong. "The reattachment and relaxation of a turbulent shear layer". In: *Journal of Fluid Mechanics* 52.1 (1972), pp. 113–135.

[8] Young. “Ventilation of Lifting Bodies: Review of the Physics and Discussion of Scaling Effects”. en. In: *Applied Mechanics Reviews* (2017), p. 38.

[9] Ruben A. Verschoof et al. “Rough wall turbulent Taylor-Couette flow. the effect of the rib height”. In: *The European Physical Journal E* (2018).

[10] Xiaojue Zhu, Roberto Verzicco, and Detlef Lohse. “Disentangling the origins of torque enhancement through wall roughness in Taylor–Couette turbulence”. In: *Journal of Fluid Mechanics* 812 (2017), pp. 279–293.